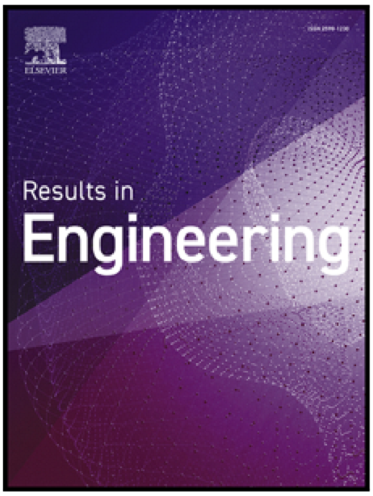

Investigation on the Interface of Additively Manufactured Bimetallic Structure: A Molecular Dynamics Simulation

Behrouz Bagheri Vanani , Gazi Tanvir , Mahdi Sadeqi Bajestani ,
Yongho Jeon , Duck Bong Kim

PII: S2590-1230(26)01025-X
DOI: https://doi.org/10.1016/j.rineng.2026.109988
Reference: RINENG 109988

To appear in: *Results in Engineering*

Received date: 7 July 2025
Revised date: 17 February 2026
Accepted date: 8 March 2026

Please cite this article as: Behrouz Bagheri Vanani , Gazi Tanvir , Mahdi Sadeqi Bajestani , Yongho Jeon , Duck Bong Kim , Investigation on the Interface of Additively Manufactured Bimetallic Structure: A Molecular Dynamics Simulation, *Results in Engineering* (2026), doi: https://doi.org/10.1016/j.rineng.2026.109988

Highlights

In this study,

- A molecular dynamics (MD) simulation analyzes Ti-Nb interfaces in wire-arc DED deposits.
- Point defects at Ti-Nb interfaces are quantified under varying heat input.
- Cluster counts drop in lower layers but rise in upper layers at high heat inputs.
- Atomic size-mismatch-induced lattice distortion drives residual stress and loop formation.
- Substrate and layers demonstrated compressive and tensile biaxial stresses, respectively.

Investigation on the Interface of Additively Manufactured Bimetallic Structure: A Molecular Dynamics Simulation

Behrouz Bagheri Vanani[1], Gazi Tanvir[2], Mahdi Sadeqi Bajestani[3,4], Yongho Jeon[5*], Duck Bong Kim[6*]

[1] *Department of Mechanical Engineering, Tennessee Technological University, Cookeville, TN, USA*
[2] *School of Environmental, Civil, Agricultural, and Mechanical Engineering, University of Georgia, Athens, GA, 30602, USA*
[3] *UHasselt, The Transportation Research Institute (IMOB), Martelarenlaan 42, Hasselt 3500, Belgium*
[4] *UHasselt, School of Transportation Sciences, Agoralaan, Diepenbeek 3590, Belgium*
[5] *Department of Mechanical Engineering, Ajou University, Suwan, Gyeongii-do, South Korea*
[6] *School of Environmental, Civil, Agricultural, and Mechanical Engineering, University of Georgia, Athens, GA 30602, USA*

*Corresponding Authors: Yongho Jeon (princaps@ajou.ac.kr) and Duck Bong Kim (DBKim@uga.edu)

Abstract

Multilayer depositions with varying interface behaviors affect the mechanical properties of deposited materials, so atomic-scale deposition mechanisms provide a better understanding of material behavior under multiple diffusion conditions. In this research, molecular dynamics is applied to investigate the behavior of the interface in Ti6Al4V-NbZr1 bimetallic structure deposited by wire-arc directed energy deposition (W-DED) in various heat input conditions. In addition, the interactions between the bimetallic structure and the distribution and size of dislocation loops are studied during deformation. It was found that the nano-melting pool forms before solidification, and the crystal growth proceeds by directional solidification, which can be equiaxed or columnar. Interdiffusion of the system shows asymmetrical diffusion behavior, and Nb atoms show a greater tendency to diffuse into the matrix in higher heat input conditions. According to the cluster analysis, the cluster number decreases from 76138 to 75720 for the first deposited layer, whereas it increases from 88046 to 90309 for the final deposited layer as heat input increases. Surface roughness decreases from 1.6 to 0.9 Å while the interface width increases from 30 to 50 Å as the heat input increases. It was concluded that atomic-size mismatch-induced lattice distortion enhances residual stress, resulting in dislocation loops. The formation of numerous 1/6 <112> Shockley and 1/2 <111> interstitial dislocation loops, along with a low amount of <100> and mixed loops, was also observed. At the substrate-interface, the biaxial stress is compressive, whereas the deposited layers exhibit tensile behavior.

Keywords: Molecular dynamics; Wire-arc directed energy deposition; Interface; Microstructure; Dislocation type.

1. Introduction

Niobium (Nb) alloys are recognized as a widely applicable material in elevated-temperature environments, such as nuclear reactors, due to their capability to maintain strength at elevated temperatures, long-term thermal creep strength, and negligible neutron absorption cross-section [1-3]. Nb–1wt%Zr is a key Nb alloy that continues to be a significant candidate for advanced nuclear applications. On the other hand, titanium (Ti) alloys, especially Ti6Al4V, play a prominent role in various applications across the automotive, aerospace, petrochemical, medical, and nuclear industries owing to their exceptional corrosion resistance, notable creep resistance, and high strength [4-6]. In recent advanced industrial applications, there has been an extreme request for structures with high, tailored, and location-specific behaviors, and bimetallic structures (BS) have been a satisfactory option. By introducing various metallic elements into a distinct component, a multifunctional structure can be produced [7]. For example, Ti6Al4V-NbZr1, titanium-zirconium-molybdenum (TZM), and niobium-zirconium (NbZr1) BSs can be utilized in aerospace and nuclear industries due to their high-temperature properties [8].

Different BSs have been fabricated using various traditional methods, including brazing, welding, diffusion bonding, and different solid-state methods [9-12]. Gao et al. [13] investigated the effect of heat input on the microstructure and mechanical properties of Ti6Al4V-Nb dissimilar alloys during pulsed fiber laser processing. They identified the dendritic region of titanium-rich phases and an island area of niobium-rich phases, without formation of intermetallic compounds (IMC) in the fusion zone. However, joining dissimilar materials directly may lead to undesirable characteristics, such as reduced mechanical properties, due to differences in their chemical and physical properties.

Additive manufacturing (AM) has attracted notable attention for its ability to fabricate a wide range of dissimilar structures with diverse chemical and physical properties [14]. Wire-arc directed energy deposition (W-DED) has been widely used as a direct energy deposition (DED)-based AM process to produce components with large and complex geometries using wire as the deposition material and an electric arc [15]. The most prominent benefits of W-DED compared to traditional methods include its low cost and the ability to produce large-scale parts [16]. W-DED has been widely employed for high-value, costly-to-process, and difficult-to-machine alloys, such as titanium and niobium. For instance, Jadhav et al. [17] studied the mechanical characteristics and microstructure in TZM-NbZr1 bimetallic structure manufactured by W-DED. They found that the interfacial microstructures had pores without prominent defects, such as cracks or delamination, and an IMC phase. W-DED was also used by Karim et al. [18] for the deposition of niobium alloys on the tungsten substrate to fabricate the W-Cu/Nb-Zr composite. The obtained results indicated noticeable diffusion of copper and niobium into the NbZr1 and W–Cu, respectively, without remarkable defects.

The interface has a prominent influence on the mechanical characterization of dissimilar materials [19]. In solid materials, interfaces can be between crystals of identical chemistry and structure with various orientations, called grain boundaries, or between crystals of various chemistry and/or structure and orientation, called interphase boundaries or hetero-phase interfaces [20]. Multilayer depositions with varying layer thicknesses on the atomic scale are of prime importance owing to their excellent mechanical and physical characterizations in comparison with classical materials. However, the engineering of such materials needs a knowledge of different phenomena at the atomic scale. Deposition mechanisms provide a better understanding of material behavior, since during deposition, atoms are associated with multiple diffusion conditions [21-23].

Molecular dynamics (MD) simulation has significant potential for investigating interface behaviors, interphase boundaries, defect structures, and physical characterizations [24]. Kanamori et al. [25] used MD to examine the interface zone of an epoxy resin adhesive on an aluminum (Al) alloy during cyclic fatigue. The obtained results indicated the formation of Al_2O_3 in the interface, and the 400K curing model shows the highest adhesion strength. In another attempt, Luo et al. [26] studied the performance of molybdenum-titanium interfaces utilizing MD simulations. It was found that there is an asymmetrical diffusion behavior at the interface, and temperature has a significant impact on the diffusion process. Dong et al. [27] applied MD to estimate the influence of the thickness of the layer on the mechanical characteristics of Cu-Nb metallic nanolayered composites (MNCs). An inverse size effect was detected for the strength of specimens with a layer thickness of below 2.0 nm. In another research, Yang et al. [28] developed an MD model to simulate tribological tests and nanoindentation of AM'd high-entropy alloys (HEAs) AlCoCrFe coated on aluminum. They concluded that in the interface of the coating and the substrate, increased laser heating temperature, leads to a greater amount of Al in the substrate being melted, reacting with other elements in the coating layer. Bizot et al. [29] deployed MD to study directional solidification in liquid copper inoculated with nanoparticles of tungsten. It was reported that global cooling, which reflects the thermal dynamics of AM, enables the observation of a nanoscale columnar to equiaxed transition. In addition, a classical MD model was developed by Nandy et al. [30] for the particles coalescence in AlSi10Mg alloy throughout laser AM. The simulation shows that unevenly-sized particles experience complete coalescence, whereas evenly-sized particles do not, and that the neck growth rate of AlSi10Mg particles enhance with increasing energy density of laser .

To date, a knowledge gap exists in the atomic-scale mechanisms that control the deposition process and the morphology of the structure, particularly at the interface area. In this paper, an MD simulation is employed to analyze the microstructure evolution of Ti6Al4V-NbZr1 BS, manufactured by W-DED, and to provide insights into dislocation density, interface formation, clustering, point defects, atomic diffusion, and grain size on an atomic scale. The outcomes of this research serve as a reference for further studies on various BSs manufactured by W-DED.

2. Materials and Methods

In this study, the simulation was based on our previous experimental data acquired during the fabrication of the Ti6Al4V-NbZr1 alloy using W-DED under different heat input conditions [31]. The NbZr1 alloy wire (ASTM-B392), with a diameter of 0.95 mm, was utilized for depositing on the Ti6Al4V alloy. The elemental composition of the wire and substrate is displayed in **Table 1.**

Table 1. Chemical composition of NbZr1 and Ti6Al4V [32, 33].

Alloy	Element (wt%)

	Nb	Ti	Zr	Al	V	Ta	O	W	Mo	C	Fe	N	Si	Cu
Ti6Al4V	-	Bal	-	6.17	4.02	-	0.13	-	-	0.02	0.04	0.022	-	0.12
NbZr1	Bal	-	0.8-1.2	0.005	-	0.5	0.025	0.05	0.05	0.01	0.01	0.01	0.005	-

This study categorizes deposition conditions according to heat input, which is determined by the arc current: low heat input (LHI) at 180 A, medium heat input (MHI) at 200 A, and high heat input (HHI) at 220 A. Additional details on how the heat input and energy density are calculated are available in [31]. **Table 2** shows the characteristics of the heat input conditions.

Table 2. Heat input conditions [34].

Condition	Heat input (J/mm)	Energy density (J/mm^3)	Current (A)
Low heat input	810	138	180
Medium heat input	900	153	200
High heat input	990	168	220

The schematic of the MD simulation W-DED process is presented in **Fig. 1**. The model features an 8-layer deposit of NbZr1 (red) containing 16,000 atoms, deposited on a Ti6Al4V substrate (grey), which has 77,760 atoms, aligned along the x-axis. with dimensions of 355.569× 38.1557× 97.6709 (A)^3. To evaluate the deposition and diffusion processes occurring between the particle and the workpiece, the NbZr1 particles move across the workpiece. To simulate the process, the LAMMPS code was deployed. In addition, the molecular dynamics system used potential functions for atomic interactions and employed the embedded-atomic method (EAM) [35], coupled with element-specific potential functions for Ti and Nb to model interatomic interactions [36]. The model for potential energy is a Lennard–Jones (LJ) pair with a cutoff distance $r_c = 2.1r_0$, in which r_0 is the equilibrium interatomic distance.

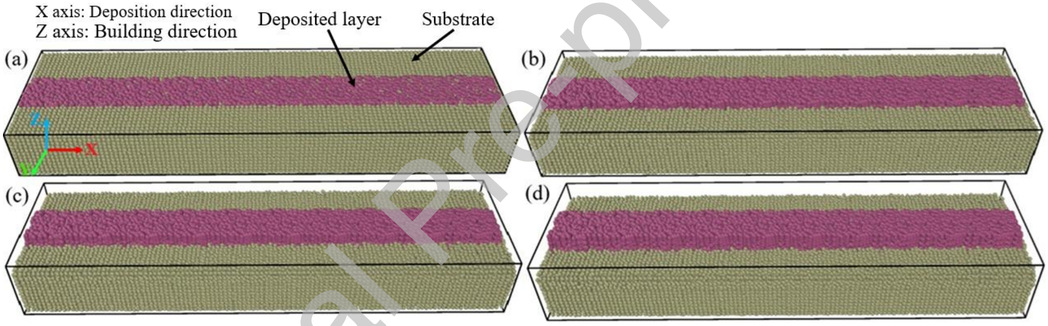

Fig. 1. A visualization of the atomic arrangement during the W-DED process of Ti6Al4V-NbZr1 for layers **(a)** two, **(b)** four, **(c)** six, and **(d)** eight.

Periodic boundary conditions (PBCs) were implemented for analyzing the three-dimensional interface model, thereby reducing the effect of boundary conditions. The substrate system was modeled with a base material of Ti in a crystal structure of hexagonal close-packed (HCP) with a constant lattice. The deposition process was performed by periodically inserting NbZr1 atoms with a constant deposition rate towards the substrate surface along the Z direction. The entered atoms in x and y coordinates were modeled randomly until all atoms were located. Eq. (1) was applied to compute the entire potential energy of the system using this technique.

$$E_{total} = \sum_i F_i(D_i) + 1/2 \sum_{i \neq j} \varphi_{ij}(r_{ij}) \qquad (1)$$

In Eq. (1), F_i is the embedded energy of atom i as a function of electron density, φ_{ij} is the pairwise potential as a function of interatomic distance (r_{ij}), and D_i denotes the electron density at atom i because of atom j distributed by r_{ij} identified as Eq. (2):

$$D_i = \sum_{j \neq i} \rho_j(r_{ij}) \qquad (2)$$

To optimize the energy of the simulation system, the conjugate gradient (CG) technique was applied before the W-DED process. To relax the system, the NPT ensemble was utilized at a low temperature of 300 K to achieve an equilibrium state. The mobilities of Ti and Nb atoms, along with related physical quantities, were observed and analyzed. In this study, only the interface region is studied. The uniform tensile strain is applied to simulate a uniaxial tensile load in the X direction at a constant strain rate of equal to 10^9 s^{-1} in the NVE ensemble. A free boundary condition was considered for stretching direction, whereas the periodic boundary conditions were considered for the remaining two directions.

The interface energy is required for shaping the interface between two main bulk phases and serves as an index of interface stability; that is, a stable interface has a low interface energy, and vice versa. The interface energy (E_{int}) for comparing the stability in different interfaces is calculated as Eq. (3) [37].

$$E_{int} = \frac{E_{tot} - E_{bulk-Nb} - E_{bulk-Ti}}{S} \qquad (3)$$

In the above equation, S and E_{tot} are the surface area and total energy of the interface, respectively. And $E_{bulk-Nb}$ and $E_{bulk-Ti}$ are the total energies of body-centered cubic Nb and HCP Ti bulks at the interface, respectively. In addition to interface mixing and crystal structure, internal stress is attributed to the quality of the deposited layers, and in thin layers, it is assigned as the atomic stress, known as the brittle-to-ductile transition (BDT) stress. The formulations for calculating it, including the interatomic forces and the kinetic energy of atoms are found in [38]. The average BDT stress, σ_{mn}^{ave}, can be calculated by Eq. (4).

$$\sigma_{mn}^{ave} = \frac{1}{N} \sum_{i=1}^{N} \sigma_{mn}^{i} \qquad (4)$$

In Eq. (4), N expresses the number of atoms, σ_{mn}^{i} is the brittle-to-ductile transition stress of the ith atom, and m and n represent the stress tensor. The normal stresses in the deposited layer are one order of magnitude larger than the shear stresses because of the residual stress. In addition, the average mean biaxial, ($\frac{\sigma_{xx}^{ave} + \sigma_{yy}^{ave}}{2}$), and average normal stresses, σ_{zz}^{ave} were determined. A smoother surface layer leads to increased oxidation and wear resistance. Therefore, the surface roughness is significant after deposition. In this case, the RMS roughness is assigned to deposited layers, as expressed in Eq. (5) [39].

$$R_q = \sqrt{\frac{\sum_{i=1}^{N} (Z_i - \bar{Z})^2}{n}} \qquad (5)$$

In the above equation, Z_i indicates the height of the exposed atoms at the top of the layer, Z is associated with the mean height of all exposed atoms, and n represents the total number of exposed atoms at the final timestep of the MD simulation.

The coordinates of atoms, history of temperature, potential energy, and stress were recorded and reported every 100 timesteps throughout the simulation [40]. VITO was applied to investigate the arrangements of atoms and their trajectories [41], while the crystallographic behavior of the structures was analyzed using polyhedral template matching (PTM), grain segmentation (GS), dislocation analysis (DXA), and common neighbor analysis (CNA) [42]. The Wigner-Seitz approach was deployed to identify the type, position, and portion of point defects, involving self-interstitial atoms (SIAs) and vacancies. A clustering study was also carried out on the recognized point defects to determine clustering fraction, size, number, and location.

3 Results and Discussion

3.1 Grain Nucleation and Morphology

Three-dimensional GS of microstructures of the Ti6Al4V-NbZr1 multi-material alloy samples in LHI condition, produced by the W-DED process, is presented in **Fig. 2**. From the start of solidification to completion, the grain size in the substrate grew by approximately 72%, due to the effect of the melting pool temperature, as illustrated in **Figs. 2(a, b)**. The base metal in the current simulation is the coarse-grained region in the heat-affected zone (HAZ) during the welding process. These features are compatible with the empirical behaviors [31]. As shown in **Fig. 2 (a)**, the bottom of the additive part is relatively closely associated with the substrate material, resulting in better heat dissipation conditions. The increased time spent in the molten pool at high temperatures resulted in a larger temperature gradient (TG) in this area. Rapid directional solidification has a direct relationship with the crystallization process of the melting pool solidification. Furthermore, the epitaxially grown crystal grains are detected at the location where they meet the substrate. Therefore, the formation of coarse-grain crystals in the direction of the temperature gradient is anticipated (**Fig. 2(b)**).

The microstructure in the middle layers, **Figs. 2(b, c)** are also prominent with equiaxed grains of a larger size compared to those at the bottom. However, the microstructure in the upper layers differs significantly from that in the bottom layers. In other words, The grains are noticeably larger, and the equiaxed grains transform into columnar dendrites with a directional orientation at the top region. The deposition shows excellent verticality, smooth surface, high metallurgical bonding, and no detrimental defects, like cracks or collapses, in LHI condition. The cross-section exhibits a stable, high-accuracy fit. This shows that the MD model of grain growth in the melting pool would demonstrate the heterogeneous grain nucleation and growth processes in the nano-melting pool. Moreover, the exact orientation and size of the microstructural characterizations depend on various factors, such as the weld sequence, the orientation of the heat flux, or the respective position within the structure [31]. Although the experimental results confirm the simulation outcomes on the MD model of microstructure evolution, they are not entirely in agreement on the scale.

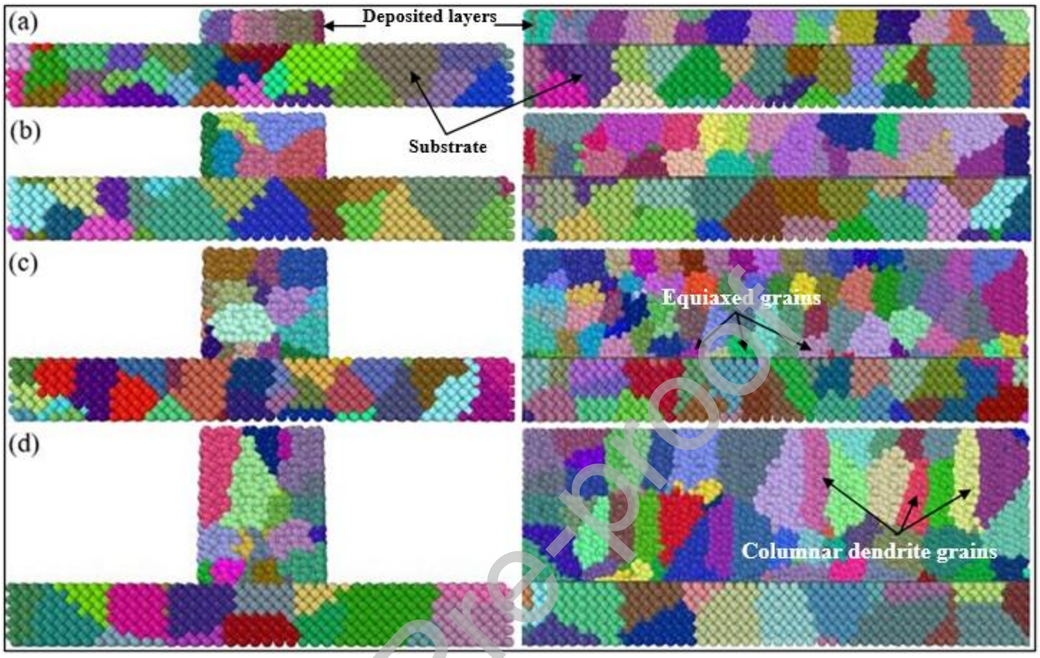

Fig. 2. Microstructure evolution and cross-section (front and side) view of GS of W-DED Ti6Al4V-NbZr1 multi-material alloy samples in LHI condition; Layer **(a)** one, **(b)** two, **(c)** five, and **(d)** eight.

A schematic illustration of the temperature gradient direction effect on grain size is demonstrated in **Fig. 3**. Increased deposition height leads to a higher average grain size. During the W-DED process, the microstructure is influenced by thermal cycles. At the beginning of the process, the preheated layer is deposited on the substrate, leading to intense heat dissipation and absorption at the surface and resulting in noticeable undercooling [43]. Heterogeneous nucleation leads to the creation of increased grain nuclei and growth in various directions on the substrate. Given the numerous grain nuclei, a competition condition begins. With the deposition of a new layer, this phenomenon will result in local thermal cycles that reheat other deposited layers. The temperature increases again, and the grains at the bottom will experience a driving force for coarsening. In addition, the portion of heat transferred by convection and radiation to the surrounding atmosphere increases with the temperature of the deposition layer.

Thermal equilibrium is prevalent in the deposition layer, and the central grains grow primarily perpendicular to it. As the previous layer cools, heat dissipation provides a preheating condition for the next layer, reducing the temperature gradient and producing a cyclic thermal field. Consequently, this solidification environment coarsens various grains in the upper layer. In addition, the equiaxed grains in the top layers, as the number of deposited layers develops, begin to grow from their surroundings. Consequently, the solidification of the melting pool on the earlier deposited weld metal enhances directional cooling and assists the epitaxial dendrites' growth, following a preference for perpendicular orientation, periodically over multiple layers. This finding aligns well with earlier research regarding the relationship between grain size and heat accumulation for each layer during the W-DED process [44-46]. Wang et al. [47] manufactured 50 layers and observed an increased growth in the fine columnar dendrite from the bottom layers to the top layers.

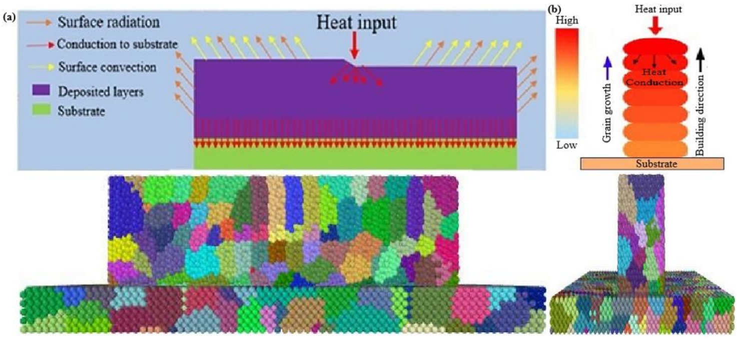

Fig. 3. Dominant heat transfer modes during the W-DED Process. **(a)** A side view, **(b)** front view of Ti6Al4V-NbZr1 alloy

3.2 Interface Characterization

The diffusion behavior of constituent elements is vital in the mechanisms of microstructural evolution in titanium systems. Diffusion bonding of Ti and its alloys usually demands high temperatures. This could cause structural deformation, grain coarsening, and deterioration of the workpiece properties. **Fig. 4** illustrates the experimental characteristics of the interlayer of W-DED Ti6Al4V-NbZr1 alloy fabricated under LHI conditions [31]. Magnified images of the interface are presented to get a better understanding of interface characterization. A strip-like region with refined equiaxed grains and a distinct width is observed in the interlayer. Some interlayer morphologies are flat, while others show curved patterns due to mutually perpendicular fill paths of adjacent deposited layers. No intermetallic compounds, pores, or cracks were observed at the interface in the higher-magnification views shown in **Fig. 4**. Discrepancies in microstructure evolution in the interface region may be associated with modifications in the HAZ.

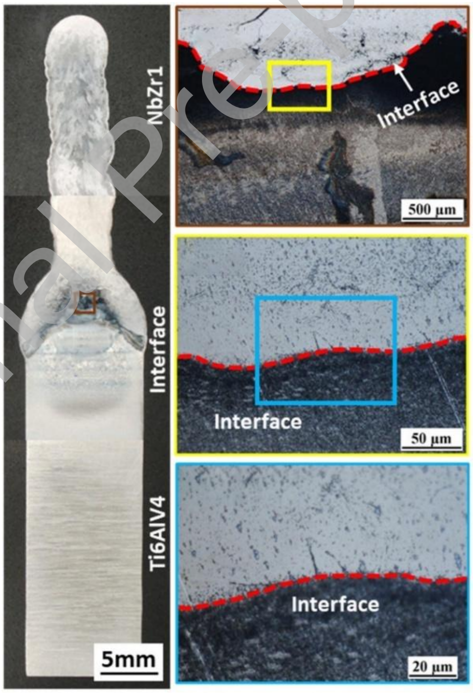

Fig. 4. Optical microscopy images of the overall cross-section for Ti6Al4V-NbZr1 BS produced in LHI condition [31].

Temperature has been identified as a key factor influencing the growth of deposited layers and their residual stress during the process. Divinski et al. [48] found that Nb diffuses more slowly than Ti in both binary and ternary Ti alloys. However, above 1000 K, the diffusion rates of both Ti and Nb are higher in the ternary alloy compared to the binary Ti alloy. A layer concentration (or coverage function) is deployed to better quantify the intermixing condition, considered from the base material to the layers. This factor is related to the proportion of a certain kind of atom to the total number in one layer. Pan et al. [49] demonstrated that homogenization of diffusion-bonded joints with a single niobium and multiple Ti/Nb/Ti interlayer occurred at ~1500 ◦C for 1 h. Raising the bonding temperature to up to 1600 ◦C resulted in no voids, attributed to the acceptable mutual solubility as well as the moderate diffusion rate of Nb. Furthermore, atomic diffusion rates are generally higher in nanocrystalline materials than in coarse-grained materials. According to Ref.

[50], coarse-grained Ti has a higher activation energy (lattice diffusion) than nanocrystalline Ti. Using Nb as an interlayer reduced the diffusion activation energy compared to lattice diffusion, approaching that of niobium diffusion in titanium grain boundaries.

The layer concentrations of atoms in the deposited layers and the substrate under various heat input conditions are displayed in **Fig. 5.** The interfacial region is subjected to the location on both sides of the interface with a higher 5% solute concentration [51]. Therefore, this figure shows that as heat input increases, interface intermixing is enhanced and substrate surface sputtering is increased. This phenomenon may be associated with a discrepancy in the composition of dissimilar metals (Ti and Nb) and with high fluid flow in the melt pool driven by the surface tension and the temperature gradient.

As a result, improving the temperature promotes the Nb diffusion, which then increases the Ti layer concentration. Furthermore, the melting point for mixed Ti-Nb, according to their binary phase diagram [52], improves as the Nb amount increases. Consequently, within the molten pool, regions with higher Nb content solidify earlier, forming island-like areas. On the contrary, regions with higher Ti content solidify afterwards and create dendritic zones, illustrated in our previous experimental study [31]. Gao et al. [13] showed that the width HAZ on the Ti6Al4V side enlarges with an improvement in the heat input owing to the ignoble phase transition temperature and thermal conductivity of the titanium alloy. This asymmetrical diffusion observation was reported in Cu-Ag [53], Al-Cu [54], and Fe-W [55] interface models.

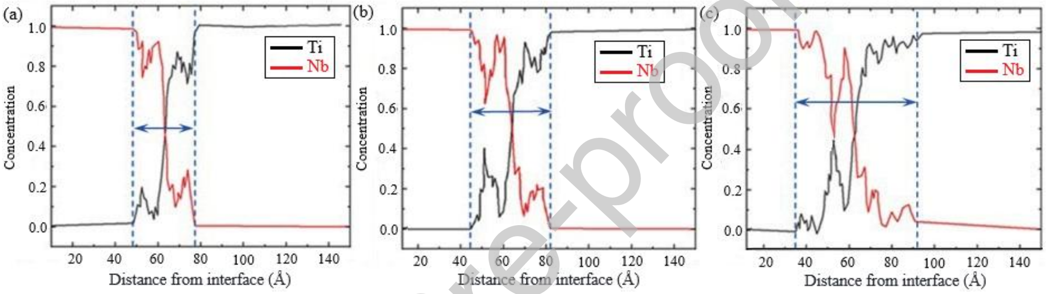

Fig. 5. Ti and Nb atom concentration along the Z-direction (interface zone) under **(a)** low, **(b)** medium, and **(c)** high heat input conditions.

In another attempt to characterize the interface, the fine-scale density variations are calculated. It is considered $\rho_i(z) =< N_z^i >/A_{xy}\Delta z$, where $< N_z^i >$ defines the average number of atoms of type i in the discrete bin, A_{xy} denotes the interfacial region, and Δz relates to the bin spacing recognized by $z-\frac{\Delta z}{2} < z+\Delta z/2$. The bin size was considered to be 1/40 of the Ti lattice constant for these profiles at the relevant temperature [56]. The fine-scale density variation at various heat input conditions is depicted in **Fig. 6**. The density peaks exhibit periodic oscillation due to the ordering structure of the crystal for Ti and Nb, which reduces slowly owing to the promotion of the Debye-Waller parameters of the crystal at the interfacial area [57]. Moreover, the density peaks continuously reduce, and some disappear as the heat input increases. This shows the predominant effect of temperature to accelerate the disordering of interfacial structure, although the mutual diffusion of atoms at the interface accounts for a tiny fraction of the entire atoms. To get a better understanding of interfacial diffusion, a magnified view of the fine-scaled density profiles is also presented in **Fig. 6**. It is obvious that the distance of Nb atoms penetrating the Ti part is longer than that of the Ti atoms penetrating the Nb part, and more Nb atoms diffuse to the Ti part. The same outcomes were mentioned by Wei et al. [55] regarding diffusion properties on the Fe-W interface system.

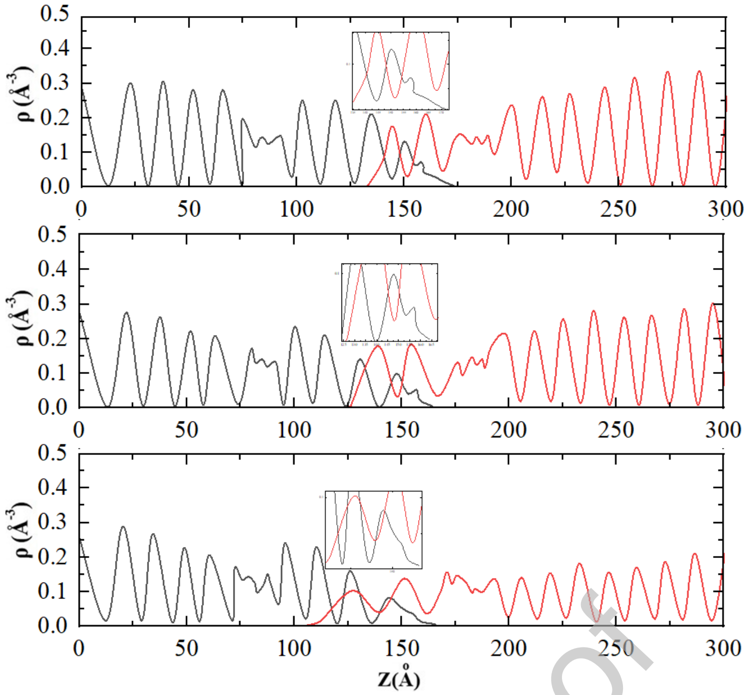

Fig. 6. The fine-scaled density variation of Ti-Nb next to the interface under **(a)** low, **(b)** medium, and **(c)** high heat input conditions.

An overview of the cross-sections of the last 8 layers in high heat input conditions at different simulation times is displayed in **Fig. 7**. As the additive deposition begins (**Fig. 7 (a)**), the atomic interaction slowly forms to develop and with moving atoms on the substrate surface, the elements are activated along the deposition path (**Fig. 7 (b)**). The heat flow to the substrate during the first-layer deposition is also higher, in contrast to the heat accumulation in the deposited layers.

Therefore, the interaction between Nb and Ti atoms increases at high temperatures, leading to an increase in Nb diffusion into the Ti phase through the initial interface, and the diffusion depth continues to increase, thereby enhancing the diffusion process (**Fig. 7 (c-e)**). **Fig. 7 (f)** displays clusters in the bottom part of the layers, providing a physical interpretation. Atoms, under continued deposition, are unable to consistently maintain their relative positions within perfect crystalline lattices. Hence, they collapse when the strain reaches a limit, and some atoms form a tiny cluster to reduce the stress. This phenomenon, along with other point defects, will be considered in the next sections.

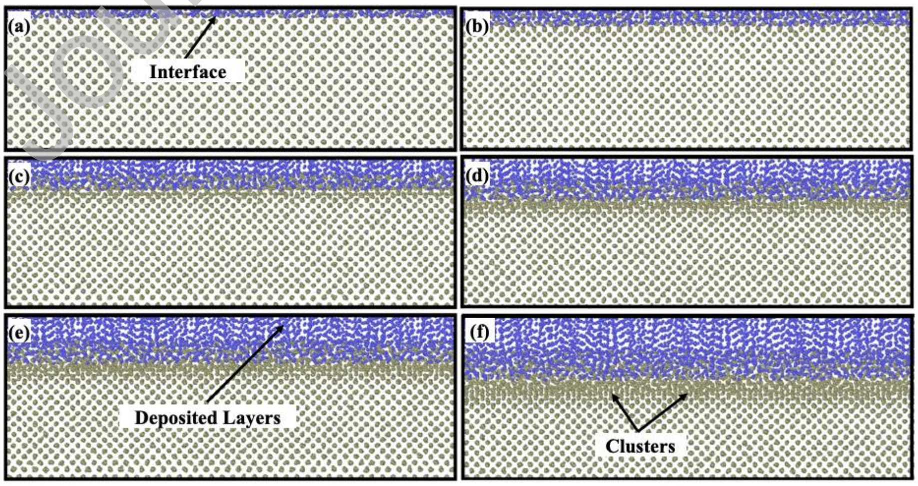

Fig. 7. The view of the atomic interdiffusion in HHI condition at different simulation times: **(a)** 1.25 ns, **(b)** 2.5 ns, **(c)** 5 ns, **(d)** 7.5 ns, **(e)** 10 ns, and **(f)** 9.6 ns.

3.3 Point Defects

Studying defects in BCC refractory metals provides a foundation for future research in structural materials and enhances our understanding of material aging. At a fundamental level, interface regions can act as sinks for defects [58]. Interactions between point defects and interfaces are crucial to material properties, as they influence microstructural stability, diffusional flow, microstructural evolution, and the precipitation and segregation of solutes or impurities [59]. It is observed that point defects demonstrate various behaviors at the interface in comparison with the crystalline solid.

Fig. 8 presents a simple schematic of the common point defects and subsequent recombination events in the current process. Forming separated point defects (like interstitials or vacancies) and clusters are the most important types of damage in the level of atoms maintained by an irradiated material during thermomechanical processes. However, the interactions of the interface with defect clusters would be qualitatively different from those with isolated interstitials and vacancies [60]. A common method for discussing the interaction between a single type of point defect, such as a vacancy, and an interface is using Eq. (6).

$$\frac{\partial C_v}{\partial t} = D_v \frac{\partial^2 C_v}{\partial X^2} + K_0 - K_{sv}(C_v - C_v^{eq}) \qquad (6)$$

In the above equation, X is the location along the normal direction to the interface, C_v relates to the concentration of vacancy. C_v^{eq} donates the thermal equilibrium of C_v, the vacancy diffusivity is defined by D_v, K_0 expresses the rate of vacancy generation, K_{sv} mentions a "lossiness" of the medium that indicates elimination of vacancies at separated sinks, including voids, dislocations, or other common defect clusters [61], and would be associated with a model vacancy mixed with interstitials. For a semi-infinite solid with $x > 0$ and an interface at $x = 0$, the steady-state condition of Eq. (6) is defined as Eq. (7).

$$C_v(x) = c_v^0 + (c_v^{eq} - c_v^0 + \frac{K_0}{K_{sv}})(1 - e^{-x\sqrt{\frac{K_{sv}}{D_v}}}) \qquad (7)$$

where C_v^0 relates to the concentration of vacancies next to the interface. For an interface with a vacancy concentration of thermal equilibrium type despite the influx of supersaturated vacancies from the adjacent solid, $C_v^0 = C_v^{eq}$, then it is a perfect vacancy sink. Therefore, the concentration of vacancy in the surroundings of the sink interface is given as Eq. (8).

$$C_v(x) = c_v^{eq} + \frac{K_0}{K_{sv}}(1 - e^{-x\sqrt{\frac{K_{sv}}{D_v}}}) \qquad (8)$$

But all interfaces do not show perfect vacancy sinks. The vacancy 'sink efficiency' η_v, explains how an interface can absorb supersaturated vacancies, as calculated by Eq. (9) [62]:

$$\eta_v = \frac{J_v}{J_v^p} \qquad (9)$$

In the above equation, J_v relates to the vacancy fluxes at the interface and J_v^p expresses the flux of vacancies into a perfect sink interface. Therefore, a sink efficiency of 1 describes a perfect sink, while zero indicates an interface with defects, like a coherent twin, which is unable to absorb any vacancies. For an interface with arbitrary sink efficiency, the solution to Eq. (6) can be written as Eq. (10).

$$C_v(x) = c_v^{eq} + \frac{K_0}{K_{sv}})(1 - e^{-x\sqrt{\frac{K_{sv}}{D_v}}}) \qquad (10)$$

As represented by the Gibbs theory of wetting [63], vacancies and SIAs fabricate clusters with different dimensions due to competition between the bulk energies and the interface. Cluster numbers are computed using OVITO based on the corresponding distance of the first RDF peak. During deposition of a layer, various SIAs and vacancies are fabricated by the thermomechanical action, and the number of surviving defects is below the initial quantity of atoms displaced.

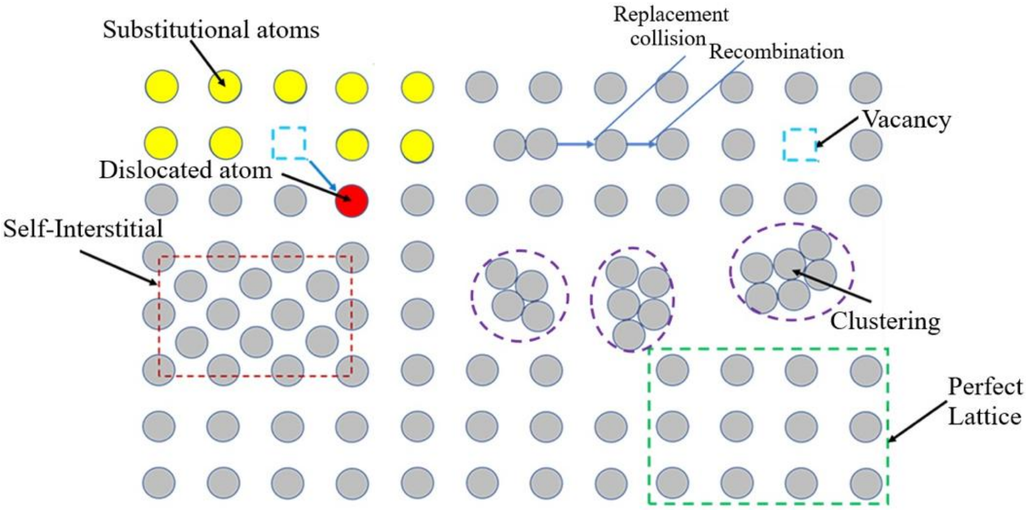

Fig. 8. Schematic illustration of the damage predicted at the interface region.

Fig. 9 presents the configuration of the damage predicted by MD at the interface in medium heat inputs. According to these results, clusters form directly within atomic displacement interfaces and can extend by capturing SIAs from the surrounding material. Although the number of clusters increases with deposited layers, the number of clusters for lower deposited layers decreases as heat input increases, whereas the reverse occurs for upper deposited layers. For example, for the first deposited layer, the cluster number decreases from 76138 to 75720, while for the final deposited layer, the cluster number increases from 88046 to 90309. It indicates that just surface atoms were remarkably distorted and separated from their initial cluster at 300 K, resulting in a slight improvement in the cluster quantity for all element kinds. **Fig. 10** shows the atomic configuration evolution of the predicted damage to determine the type, position, and quantity of point defects in various heat inputs. The summary of the calculated cluster, vacancy, and interstitial number analysis for W-DED Ti6Al4V-NbZr1 alloy is presented in **Table 3**.

As the number of layers increases, due to higher temperatures, tiny clusters merge and atoms aggregate, while at high temperatures, the diffusion of atoms in the previous layers increases, allowing clusters to move freely and their number to grow. In addition, no vacancy is observed for the first three deposited layers for various heat inputs. At higher layers, the number of vacancies decreases with higher heat inputs. However, the number of SIAs increases in higher layers and in higher heat inputs. This phenomenon may be related to high atomic interaction between deposited layers. Alexander et al. [64] concluded that vacancy clusters of different BCC materials display equivalent behavior. However, SIA clusters exhibit various behaviors on the BCC metal under consideration.

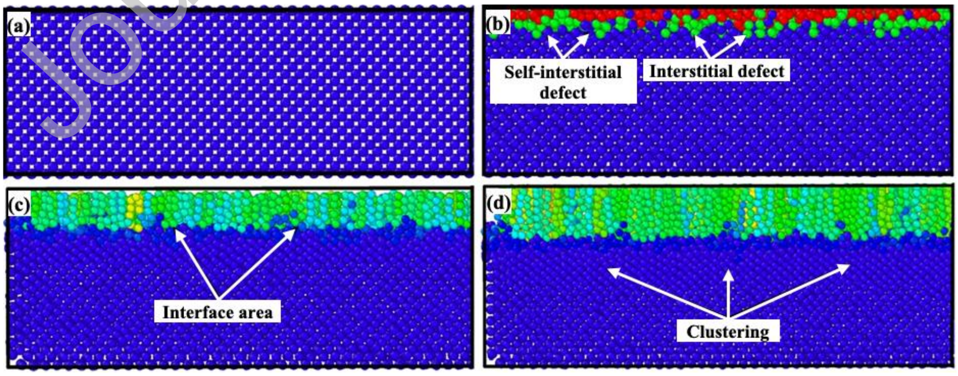

Fig. 9. Atomic configuration evolution of the damage predicted by MD at the interface region of W-DED Ti6Al4V-NbZr1 alloy in MHI condition; **(a)** perfect lattice, **(b)** formation of SIAs, **(c)** interaction of atoms in the interface, and **(d)** clustering.

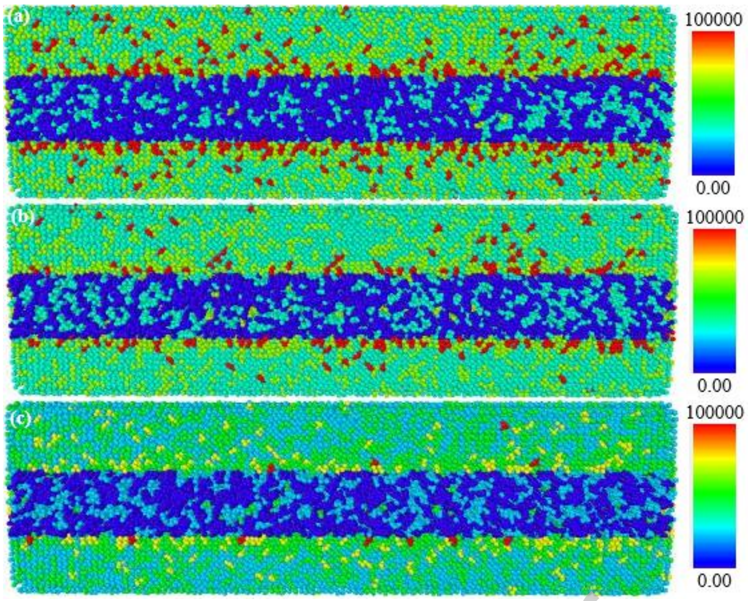

Fig. 10. Atomic configuration evolution of the damage (top view) to determine the type, location, and quantity of point defects under **(a)** low, **(b)** medium, and **(c)** high heat input conditions (The blue area is related to the deposited layers).

Table 3. A summary of cluster, vacancy, and interstitial number analysis for W-DED Ti6Al4V-NbZr1 alloy under different heat inputs.

Layer No.	**LHI**			**MHI**			**HHI**		
	Cluster number	**Vacancy number**	**Interstitial number**	**Cluster number**	**Vacancy number**	**Interstitial number**	**Cluster number**	**Vacancy number**	**Interstitial number**
1	76138	0	1530	75943	0	1700	75720	0	2000
2	77302	0	3060	76983	0	3400	76666	0	4000
3	79471	0	4590	79145	0	5100	78401	0	6000
4	81770	44	6163	81777	36	6836	81040	34	8034
5	83470	115	7765	83887	99	8599	83978	102	10102
6	85002	289	9469	85625	261	10461	86286	258	12258
7	86519	783	11493	87330	743	12643	88296	676	14676
8	88046	1608	13848	89017	1527	15127	90309	1428	17428

3.4 Phase Analysis

During the GTAW process, the driving forces for the melting pool flow include the Lorentz force, buoyancy force, and shear stress are affected by the surface tension gradient and arc pressure. Accordingly, the variation of surface tension affects the melting pool flow, resulting in the interface penetration that has a crucial effect on microstructure evolution. That is, high shear stress caused by the high surface tension gradient generates a fairly shallow deposition penetration. Thus, the small grains created by the previously deposited layer cannot be remelted, and the fabrication of small equiaxed grains inside the multi-layer deposition will be approached by the combination of thermal undercooling (pulsed arc) and constitutional supercooling (niobium addition).

The phase structure of the nanocomposite and the chemical composition might alter during an AM process. If an interstitial atom created in one phase diffuses to another, the variation in the chemical structure of that second phase occurs, which may result in either complexion (new phases) at the interface [65] or even an entire transformation of the full phase into a new phase. Therefore, anticipating the microstructure evolution is related to understanding the interaction of phases as the nanocomposite evolves under the process.

Fig. 11 shows the close-up view of the atomic structure evolution of the W-DED Ti6Al4V-NbZr1 system. As **Fig. 11 (a)** shows, before the deposition process, the interfacial atoms have a regular arrangement. The atoms are color-coded based on their structure. In the interfacial area, the atoms with local BCC and HCP stacking are colored blue and red, respectively. When the deposited layer is applied, both the Ti substrate and Nb deposition atoms interact with each other at the initial stage (**Fig. 11 (b)**). In higher layers (**Figs. 11 (c, d)**), the plasticity begins with the nucleation of dislocations and then glides along various slip systems and arrives at the interface. As the layer deposition continues, **Fig. 11 (e, f)**, higher dislocations and twining are nucleated from the surface of previous layers and interact with the interface, resulting in higher atomic-scale interaction and deformation. Therefore, the Ti-NbZr1 coherent interface, with an increase in the deposited layers, interacts with the dislocations, slip systems, and twining from the surface of Ti6Al4V and facilitates the plastic formation and inner-interaction of atoms. In addition, increased crystallization into the BCC structure was observed with an increase in the deposition process. The phase transformation happens because atoms at the interface between two grains undergo deposition and then convert into a temporary BCC, influenced by changes in in-plane grain misorientation and the relative rotation between the grains. Similar observations are reported in MD simulations for HCP crystals [66].

The initial dendritic phase was recognized to have a BCC (Nb, Ti) microstructure. According to Zhou et al. [67], the influence of the niobium filler in the weld is mostly related to its consumption rather than its barrier. In addition, based on the experimental study [68], the Ti-Nb interface primarily comprises α-Ti, β-Ti, and (Nb, Ti) solid-solution, without an intermetallic phase, owing to the complete solubility of Ti and Nb in the binary phase diagram. The mechanism through which the dislocation nucleated at the interface is investigated in Section 3.5.

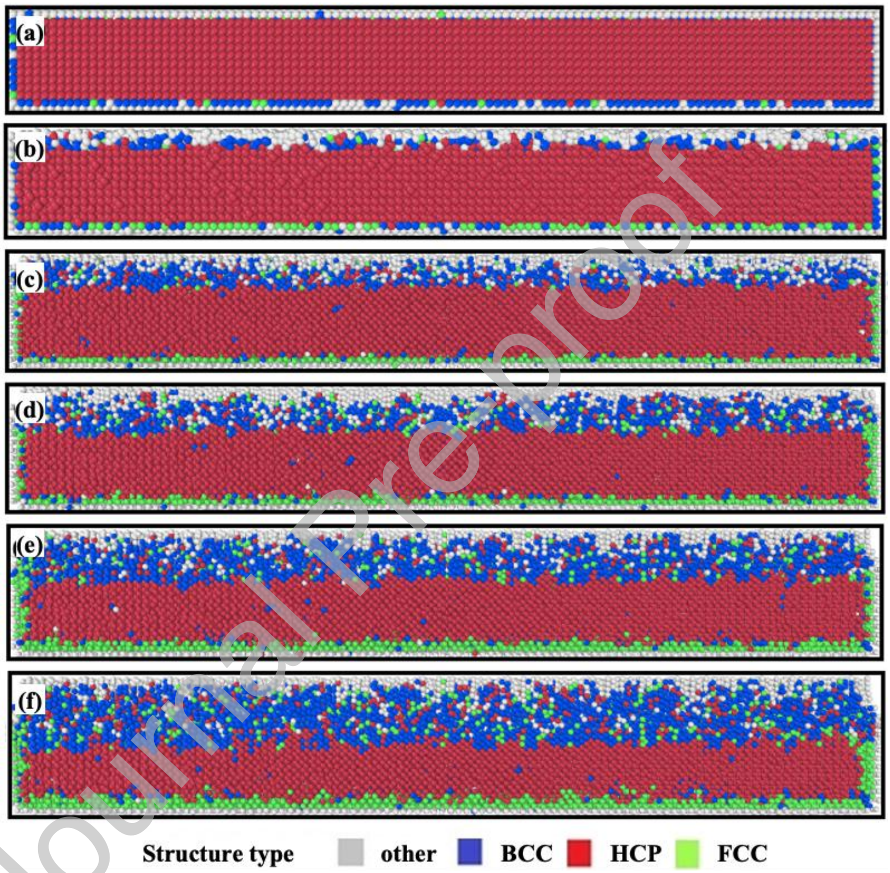

Fig. 11. Atomic configuration evolution of the phase variation by MD during the W-DED process of Ti6Al4V-NbZr1; **(a)** substrate, layers **(b)** one, **(c)** two, **(d)** four, **(e)** six, and **(f)** eight.

The surface morphology of the W-DED Ti6Al4V-NbZr1 alloy in various heat inputs at the final step is presented in **Fig. 12**. The adatom diffusion has been determined as a crucial factor in controlling the surface morphology and quality during the epitaxial growth condition [69]. As illustrated in **Fig. 12 (a)**, the surfaces of the deposited layers are not flat or smooth due to the low heat input, at which the diffusion and interaction of atoms cannot be noticeable and have low atom movement. Given increased Nb diffusion as heat input increases, the interaction of materials at the interface increases, and the number of vacancies reduces; consequently, the surface quality increases (**Fig. 12 (c)**). Similar results were reported by Hwang et al. [70] for copper cluster deposition on a Si substrate and by Mes-adi et al. [71] for Cu film on Si. Table 4 shows the roughness of the deposited thin film as a function of the heat input. It can be seen clearly that the value of surface roughness decreases slightly when the heat input increases from low to high; therefore, the heat input has an important effect on the surface roughness of deposited layers.

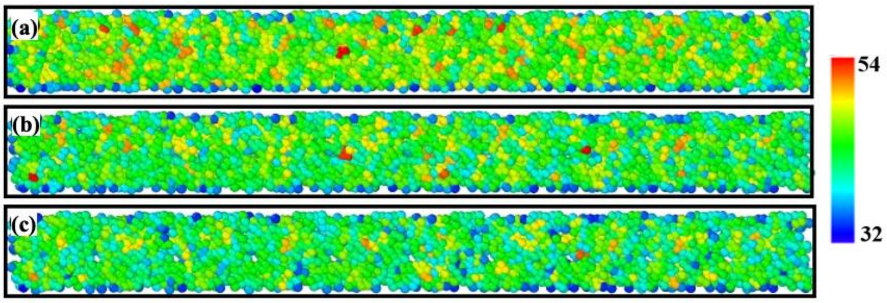

Fig. 12. Morphology of eight layers on the substrate under **(a)** low, **(b)** medium, and **(c)** high heat input conditions (Color coding is representative for atom height (Å)).

Table 4. The surface roughness under different heat inputs.

Heat input	LHI	MHI	HHI
Roughness (Å)	1.6	1.2	0.9

3.5 Dislocation Analysis

Cyclic deformation significantly alters vacancy cluster and dislocation loop size and morphology [72]. Vacancies typically coalesce into 3D voids to minimize energy, whereas interstitials cluster into planar arrangements that collapse into prismatic dislocation loops. These loops generate long-range deformation fields. Spanning the interval between SIAs, cluster atoms, and nanometric-sized dislocation types, generating experimental results is challenging due to the high-resolution demands to analyze atomic-scale objects. Filkar et al. [73] found that vacancy dislocation loops in BCC materials are metastable at low temperatures, requiring high temperatures to transform into voids. Research indicates that compressive strain enhances the transition from nanosized vacancy clusters to dislocation loops, while tensile strain favors the reverse [74]. Furthermore, Filkar et al. [73] observed that dislocation loop energy is nearly proportional to dislocation length, and vacancy cluster energy is nearly proportional to the cluster's surface area. Therefore, to further analyze the deformation mechanism of the tensile test process of Ti6Al4V-NbZr1, defect atom analysis and DXA were applied to the deposition process. The results are presented in **Fig. 13**. Generally, dislocation nucleation occurs in the melted subsurface and propagates along the interface. Then, dislocations begin to propagate, starting the grain boundaries, and a dense pattern of dislocations is produced and expanded across the microstructure by the appearance of stacking faults [75]. Once the top surface is influenced by the arc energy, the melting process initiates and propagates into the material. Simultaneously, the melting start point is considered a promising site for dislocation nucleation (**Fig. 13 (a)**). As the process continues, the rapid accumulation of Shockley partial dislocation densities occurs, and dislocations propagate from the grain boundary region. In higher heat inputs (**Fig. 13 (b, c)**), the density of dislocations at the interface reduces significantly, and the number of disordered atoms at the interface increases. The increased dislocation density is caused by the significant number of dislocations (mostly 1/6 <112> Shockley), and fine grains with numerous grain boundaries in LHI condition hinder the mobility of dislocations. As a result, a development in the dislocation density is anticipated.

As heat input increases, the grain size grows, and the number of grain boundaries reduces; hence, the mobility of dislocations increases, and their density decreases [76]. Additionally, the incoherent interface may serve as an effective nucleation site for dislocations, leading to plastic deformation. The atoms in the incoherent area at the interface exhibit weaker interfacial interactions due to the larger bond lengths of interfacial atomic pairs. Accordingly, the incoherent areas in the NbZr1 atomic arrays at the interface are considered the weakest interfacial areas in terms of atomic interaction. During the deformation process, the interfacial shear resistance along these areas is low, so the Shockley dislocations may preferentially nucleate from these areas.

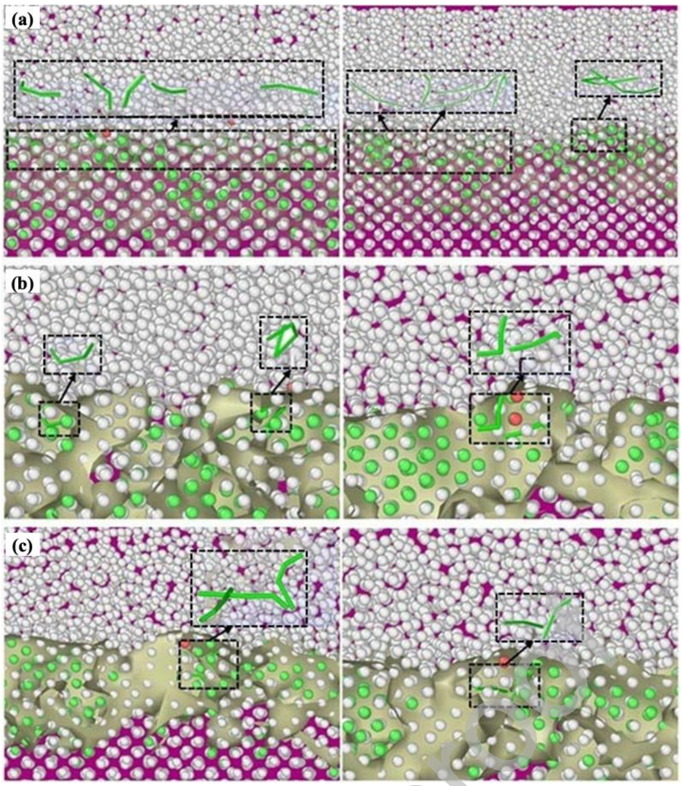

Fig. 13. Defect atoms and dislocation lines of W-DED Ti6Al4V-NbZr1 alloy along the x-axis for **(a)** low, **(b)** medium, and **(c)** high heat input conditions.

The appearance of a dislocation loop is fundamentally influenced by lattice distortion resulting from atomic-size mismatch and causes the expansion of residual stress. Due to a mismatch in the atomic size in the solid solution, the lattice exhibits distorted behavior, leading to a concentration of localized stress that may result in residual stress under specific conditions. **Fig. 14** demonstrates the generation of dislocation loops in W-DED Ti6Al4V-NbZr1 alloy in various heat inputs. The number of dislocation loops varied with heat input, and different dislocation loops could be detected when different heat inputs were applied during deposition. In this case, three kinds of interstitial dislocation loops, like <100> loops, 1/2<111> loops, and mixed interstitial dislocation loops, are observed under different conditions. The quantity of <100> interstitial dislocations in comparison with the quantity of 1/2<111> interstitial dislocation loops is much less, which is in agreement with the MD analysis [77] and experimental outcomes [78].

In addition, the density functional theory (DFT) study reported by Alexander et al. [63] indicated that the formation energy of interstitial dislocation loops with b = 1/2 <111> is lower than that of b = <100> interstitial dislocation loops, including the identical number of interstitials. The free energy of the <100> improves more quickly than that of the 1/2 <111>. Accordingly, forming 1/2<111> interstitial dislocation loops is easier than that of <100>. It has been demonstrated by Chu et al. [79] that the interactive energy, based on a power-law relationship, decays quickly for a dislocation loop than for a straight dislocation. In addition, the interactive energy is associated with the ratio d/a; where a is the diameter of the loop and d is the distance to the interface. The influence of dislocation loops on the tribological and mechanical behaviors of refractory alloys was also investigated by Zhang et al. [80]. It was found that atomic-size mismatch-induced lattice distortion increases residual stress, generating dislocation loops and thereby promoting the material's thermal conductivity. Therefore, the fabrication of dense oxide layers is increased by facilitating oxygen diffusion and uniformity of the temperature distribution.

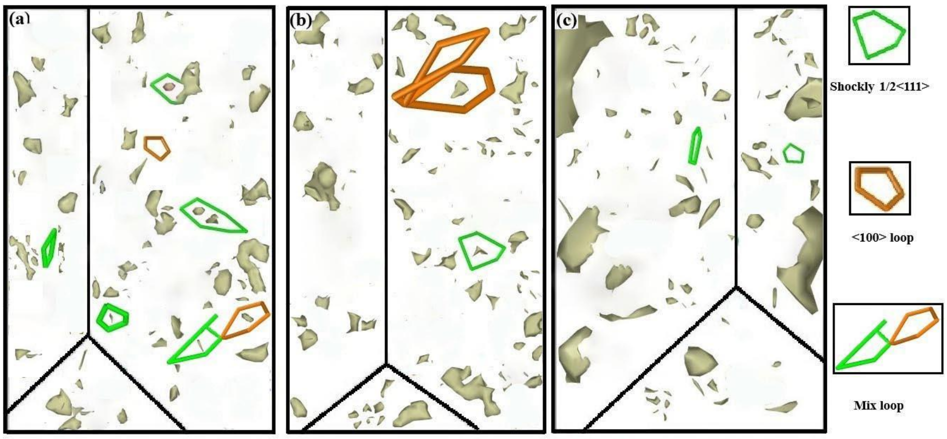

Fig. 14. The defect and loop dislocation distributions during the tensile test for W-DED Ti6Al4V-NbZr1 for **(a)** low, **(b)** medium, and **(c)** high heat input conditions.

3.6 Mechanical Properties

Dislocations and their interaction with alloying elements are of interest due to their influence on mechanical behavior. As crystalline defects, dislocation loops can enhance mechanical properties by affecting dislocation movement, modifying stress distributions, and enhancing heat transfer [81]. Their abundance suggests significant plastic deformation in the as-cast state, resulting from dislocation multiplication and motion. These loops improve work-hardening through dislocation interactions, thus improving the alloy's mechanical performance [82]. Further analysis of how multilayer deposition affects the mechanical properties, specifically the normal and the average mean biaxial stresses in LHI, is shown in **Fig. 15**. The trend of curves is identical for all layers, and the biaxial stress of the samples reduces in the substrate and then increases at the interface and deposited region. Regarding normal stress, the curves show a trend toward reduced substrate stress, while remaining relatively constant near the interface. Additionally, all layers exhibit a falling behavior with fluctuations. In fact, the deposited atoms compress the substrate material; however, the deposition-substrate interface shows less tensile behavior due to high atom diffusion and intermixing. At higher layers, biaxial stress develops in the deposited layer, with no noticeable effect on its normal stress. These outcomes agree with the report by Amini et al. [83] on MD analysis of Ti-TiN on FeCrNi (001).

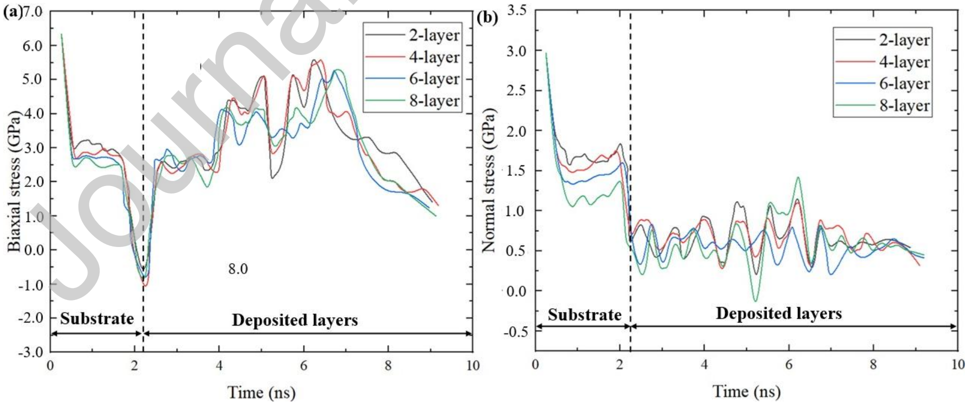

Fig. 15. The stresses of W-DED Ti6Al4V-NbZr1 alloy under low heat inputs. **(a)** Average mean biaxial stress, **(b)** Average normal stress.

4. Conclusions

In the current study, the interface characterization of the Ti6Al4V-NbZr1 BS manufactured by W-DED in different heat input conditions (LHI, MHI, and HHI) was investigated by MD simulation. The microstructure indicated the formation of coarse, equiaxed grains into columnar dendrite grains, and with increasing deposition height, the average grain size increased. The interface analysis revealed an increase in the interface width from 30 to 50 Å as the heat input increased, attributed to increased Nb atom diffusion. The number of clusters decreases from 76138 to 75720 in the first layers, while it increases from 88046 to 90309 in the final layer. The temperature plays a significant role in determining the quality and smoothness of the deposited surface. The mobility and movement of dislocation (mostly 1/6 <112> Shockley in this study) increase with higher heat inputs. Three kinds of interstitial dislocation loops, including <100>, 1/2<111> l, and mixed interstitial dislocation loops, were detected in different heat conditions. At the substrate-interface, the biaxial stress exhibits compressive behavior, whereas it transforms to tensile in the deposited layers. While the deposited layers show a tensile trend. Dislocation reactions and grain boundary deformation primarily govern the main plastic behavior, resulting in the development of new structures.

While all-atom MD accurately models material properties, its application is limited by computational cost and accessible time/length scales. Real-time simulations, crucial for nanotechnology and materials research, will enable tracking processes during experiments. Collaboration between computational and experimental researchers will validate simulations, yielding new insights for tailored materials and efficient nanofabrication. Overall, these advancements will significantly expand MD's impact across science and technology.

Acknowledgements

This work was supported by the National Research Foundation of Korea (NRF) grant funded by the Korean government (MSIT) (No. RS-2024-00346883).

Declaration of Competing Interest

The authors declare no competing interests.

Data Availability Statement

The data will be made available upon request.

Credit Author Statement

Behrouz Bagheri Vanani: Data curation, Formal analysis, Investigation, Methodology, Software, Writing – original draft; **Gazi Tanvir:** Formal analysis, Visualization, Writing – review & editing; **Mahdi Sadeqi Bajestani:** Investigation, Validation, Visualization, Writing – review & editing; **Yongho Jeon:** Formal analysis, Funding acquisition, Supervision, Writing – review & editing; **Duck Bong Kim:** Conceptualization, Formal analysis, Project administration, Resources, Writing – review & editing.

Reference

1. A. Sarkar, R. Kapoor, A. Verma, J.K. Chakravartty, A.K. Suri, Hot deformation behavior of Nb–1Zr–0.1C alloy in the temperature range 700–1700 ^{0}C, J. Nuclear. Mater. 422 (2012) 1–7. http://dx.doi.org/10.1016/j.jnucmat.2011.11.064
2. M. Sankar, R.G.Baligidad, A.A.Gokhale, Effect of oxygen on microstructure and mechanical properties of niobium, Mater. Sci. Eng. A. 569 (2013) 132–136. http://dx.doi.org/10.1016/j.msea.2013.01.025
3. J.P. Hankwitz, CH. Ledford, Christopher Rock, Scott O'Dell and Timothy J. Horn, Electron Beam Melting of Niobium Alloys from Blended Powders, Mater. 14 (2021) 5536. https://doi.org/10.3390/ma14195536
4. X.L. Gao, L.J. Zhang, J. Liu, J.X. Zhang, Effects of weld cross-section profiles and microstructure on properties of pulsed Nd:YAG laser welding of Ti6Al4V sheet, Int. J. Adv. Manuf. Technol. 72 (2014) 895–903. https://doi.org/10.1007/s00170-014-5722-x
5. G. Casalino, M. Mortello, A FEM model to study the fiber laser welding of Ti6Al4V thin sheet, Int. J. Adv. Manuf. Technol. 85 (2016) 1339–1346. https://doi.org/10.1007/s00170-015-8298-1
6. A.M. Beese, B.E. Carroll, Review of mechanical properties of Ti-6Al-4V made by laser-based additive manufacturing using powder feedstock, JOM 68 (2016). https://doi.org/10.1007/s11837-015-1759-z
7. S. Jadhav, G. Tanvir, Md. Abdul Karim, S. Islam, S. Do Noh, D.B. Kim, Microstructures and mechanical behaviour of bimetallic structures of tungsten alloy (90WNiFe) and nickel alloy (In625) fabricated by wire-arc directed energy deposition, Virtual. Physic. Prototyping. 19:1 (2024) 2370957. https://doi.org/10.1080/17452759.2024.2370957
8. S. Islam, G-J Seo, Md.R.U. Ahsan, H. Villarraga-Gómez, H-J Lee, D.B. Kim, Investigation of Microstructures, Defects, and Mechanical Properties of Titanium-Zirconium-Molybdenum Alloy

Manufactured by Wire Arc Additive Manufacturing, Int. J. Ref. Metal. Hard. Mater. 110 (2023) 106042. https://doi.org/10.1016/j.ijrmhm.2022.106042

9. A. Abdollahzadeh, B.B. Vanani, A.M. Morghmaleki, A.O. Moghaddam, A.R. Eivani, Advancements in joining Al-Zn-TiC-Mg composites using friction stir welding process: Influence of traverse speed, J. Comp. Mater. 58(26) (2024) 2757-2779. https://doi.org/10.1177/00219983241274502
10. B. Bagheri, A. Abdollahzadeh, A. Shamsipur, A Different Attempt to Analysis Friction Stir Spot Welding of AA5083-Copper Alloys, Mater. Sci. Technol. 39(9) (2023) https://doi.org/10.1080/02670836.2022.2159633
11. A. Abdollahzadeh, B.B. Vanani, H. Koohdar, A.A. Babereh, M. Yeganeh, Multi-pass Friction Stir Welding of Al–TiC–Zn–Mg Composite: Microstructure and Mechanical Characteristics. Metall. Micro. Anal. 13 (2024) 601-623. https://doi.org/10.1007/s13632-024-01117-7
12. A. Abdollahzadeh, B.B. Vanani, H. Koohdar, H.R Jafarian, Influence of Variation Ambient System on Dissimilar Friction Stir Welding of Al Alloy to Mg Alloy by the Addition of Nanoparticles and Interlayer, Metal. Mater. Int. 30 (2024) 2830-2852. https://doi.org/10.1007/s12540-024-01670-4
13. X-L. Gao, J. Liu, L-J. Zhang, Effect of heat input on microstructure and mechanical properties of pulsed laser welded joints in Ti6Al4V/Nb dissimilar alloys, Int. J. Adv. Manuf. Technol. 94 (2018) 3937-3947. https://doi.org/10.1007/s00170-017-1134-z
14. R. Ghanavati, H. Naffakh-Moosavy, Additive Manufacturing of Functionally Graded Metallic Materials: A Review of Experimental and Numerical Studies, J. Mater. Res. Technol. 13 (2021) 1628-1664. https://doi.org/10.1016/j.jmrt.2021.05.022
15. X. Bai, P. Colegrove, J. Ding, X. Zhou, CH. Diao, PH. Bridgeman, J.R. Hönnige, H. Zhang, S. Williams, Numerical analysis of heat transfer and fluid flow in multilayer deposition of PAW-based wire and arc additive manufacturing, Int. J. Heat. Mass. Transfer. 124 (2018) 504–516. https://doi.org/10.1016/j.ijheatmasstransfer.2018.03.085
16. A.S. Yildiz, K. Davut, B. Koc, O. Yilmaz, Wire arc additive manufacturing of high-strength low alloy steels: study of process parameters and their influence on the bead geometry and mechanical characteristics, Int. J. Adv. Manuf. Technol. 108 (2020) 3391-404. https://doi.org/10.1007/s00170-020-05482-9
17. S. Jadhav, Md. Abdul Karim, D.B. Kim, Bimetallic structure of TZM and NbZr1 fabricated by wire-based directed energy deposition, Mater. Letter 356 (2024) 135605. https://doi.org/10.1016/j.matlet.2023.135605
18. Md. Abdul Karim Y. Jeon, D.B. Kim, Trailblazing multi-material structure: Niobium alloy to tungsten-copper composite using wire-arc additive manufacturing, Mater. Letter 375 (2024) 137246. https://doi.org/10.1016/j.matlet.2024.137246
19. B. Bagheri, M. Abbasi, F. Sharifi, A. Abdollahzadeh, Investigation into Novel Multipass Friction Stir Vibration Brazing of Carbon Steels, Materials and Manufacturing Processes, 37(8) (2022) 921-932. https://doi.org/10.1080/10426914.2021.2006220
20. I.J. Beyerlein, M.J. Demkowicz, A. Misra, B.P. Uberuaga, Defect-interface interactions, Prog. Mater. Sci. 74 (2015) 125–210, http://dx.doi.org/10.1016/j.pmatsci.2015.02.001
21. A. Abdollahzadeh, B.B. Vanani, M. Abbasi, M. Mohammadkhah, S. Klinge, Numerical Investigation of Heat Input Effects in Additive Manufacturing of Molybdenum Alloys, J. Mater. Res. Technol, 41, 3133–3144, 2026. https://doi.org/10.1016/j.jmrt.2026.01.192
22. B.B. Vanani, G. Tanvir, M.S. Bajestani, Y. Jeon, D.B. Kim, Coupled thermo-mechanical finite simulation of heat treatment effects in wire arc additively manufactured Inconel 625, J. Mater. Res. Technol, 2026. https://doi.org/10.1016/j.jmrt.2025.12.243

23. D.P. Adams, Reactive multilayers fabricated by vapor deposition: a critical review, Thin Solid Films 576 (2015) 98–128, https://doi.org/10.1016/j.tsf.2014.09.042
24. B.B. Vanani, M. Abbasi, M. Givi**,** Compressive behavior of octet lattice made by carbon fiber reinforced polymer composite hollow struts: molecular dynamic simulation, Multiscale. Multidiscipline. Model. Exp. Des. (2025), 8(2). https://doi.org/10.1007/s41939-024-00607-z
25. K. Kanamori, Y. Kimoto, SH. Toriumi, A. Yonezu, On the cyclic fatigue of adhesively bonded aluminium: Experiments and molecular dynamics simulation, Int. J. Adhesion. Adhesives. 107 (2021) 102848. https://doi.org/10.1016/j.ijadhadh.2021.102848
26. M. Luo, L. Liang, L. Lang, SH. Xiao, W. Hu, H. Deng, Molecular dynamics simulations of the characteristics of Mo/Ti interfaces, Comput. Mater. Sci. 141 (2018) 293–301. https://doi.org/10.1016/j.commatsci.2017.09.039
27. SH. Dong, T. Chen, S. Huang, N. Li, C. Zhou, Thickness-dependent shear localization in Cu/Nb metallic nanolayered composites, Scrip. Mater. 187 (2020) 323–328. https://doi.org/10.1016/j.scriptamat.2020.06.049
28. X. Yang, J. Zhang, S. Sagar, T. Dube, B-G. Kim, Y-G. Jung, D.D. Koo, A. Jones, J. Zhang, Molecular dynamics modeling of mechanical and tribological properties of additively manufactured AlCoCrFe high entropy alloy coating on aluminum substrate, Materials Chemistry and Physics 263 (2021) 124341. https://doi.org/10.1016/j.matchemphys.2021.124341
29. Q. Bizot, O. Politano, F. Baras, V. Turlo, Directional solidification of Cu with dispersedWnanoparticles: A molecular dynamics study in the context of additive manufacturing, Materi. 36 (2024) 102140. https://doi.org/10.1016/j.mtla.2024.102140
30. J. Nandy, S. Sahoo, N. Yedla, H. Sarangi, Molecular dynamics simulation of coalescence kinetics and neck growth in laser additive manufacturing of aluminum alloy nanoparticles, J. Molecule. Model, 26 (2020). https://doi.org/10.1007/s00894-020-04395-4
31. S. Jadhav, M.S. Bajestani, S. Islam, Md. Abdul Karim, CH.J. Kim, H-J. Lee, Y.T. Cho, D.B. Kim, Materials characterization of Ti6Al4V to NbZr1 bimetallic structure fabricated by wire arc additive manufacturing, Mater. Today. Commune. 36 (2023) 106934. https://doi.org/10.1016/j.mtcomm.2023.106934
32. S.M Sawant, N.K. Jain, S.H. Nikam, Theoretical modeling and finite element simulation of dilution in micro-plasma transferred arc additive manufacturing of metallic materials, Int. J. Mech. Sci. 164 (2019) 105166. https://doi.org/10.1016/j.ijmecsci.2019.105166
33. S. Islam, M.R. Ahsan, G. Seo, H. Lee, T. Park, F. Pourboghrat, D.B. Kim, Investigations of microstructure and mechanical properties in wire arc additively manufactured niobium-zirconium alloy, Adv. Eng. Mater. (2023). https://doi.org/10.1002/adem.202201633
34. B.B. Vanani, S. Islam, M.S. Bajestani, Y. Jeon, D.B. Kim, Microstructure evolution and mechanical behaviors of Ti6Al4V/NbZr1 bimetallic additively manufactured structure: A molecular dynamics simulation, Int. J. Mater. Res. Technol. 37 (2025) 3466-3477. https://doi.org/10.1016/j.jmrt.2025.07.025
35. G. Bonny, N. Castin, J. Bullens, A. Bakaev, T.C.P. Klaver, D. Terentyev, On the mobility of vacancy clusters in reduced activation steels: an atomistic study in the Fe–Cr–W model alloy, J. Phys.: Condensed Matter 25 (2013) 315401, https://doi.org/10.1088/0953-8984/25/31/315401
36. D. Farkas, C. Jones, Interatomic potentials in ternary Nb-Ti-Al alloys, Model. Simul. Mater. Sci. Eng. 4 (1996) 23–32. http://dx.doi.org/10.1088/0965-0393/4/1/004

37. Y.J. Shen, S.T. Mi, L. Sun, L.Y. Yang, H.R. Gong, Mechanical properties and dislocation evolution of Cu–Fe interfaces from molecular dynamics simulation, Mater. Chem. Physic. 262 (2021) 124270. https://doi.org/10.1016/j.matchemphys.2021.124270
38. Z.H. Hong, S.F. Hwang, T.H. Fang, Atomic-level stress calculation and surface roughness of film deposition process using molecular dynamics simulation, Comput. Mater. Sci. 48 (2010) 520–528, https://doi.org/10.1016/j. commatsci.2010.02.018
39. L. Zhang, H. Yan, K. Sun, S. Liu, Z. Gan, Molecular dynamics simulations of AlN deposition on GaN substrate, Mol. Phys. 117 (2019) 1758–1767, https://doi.org/10.1080/00268976.2019.1587025
40. P. Li, L. Wang, S. Yan, M. Meng, K. Xue, Temperature effect on the diffusion welding process and mechanism of B2–O interface in the Ti2AlNb-based alloy:A molecular dynamics simulation, Vacuum 173 (2020) 109118. https://doi.org/10.1016/j.vacuum.2019.109118
41. A. Stukowski. Visualization and analysis of atomistic simulation data with OVITO–the Open Visualization Tool. Model. Simul. Mater. Sci. Eng. 18(1) (2009) 015012. https://doi.org/10.1088/0965-0393/18/1/015012
42. D. Yang, H. Liu, Q. Jiang, Y. Jiang, X. Wang, W. Yang, Atomic-level understanding of weakening crystallization in additive manufactured ternary Fe-based metallic glasses with Ni addition, J. Non-Cryst. Solids. 582 (2022) 121435. https://doi.org/10.1016/j.jnoncrysol.2022.121435
43. C. Zhang, M. Gao, X. Zeng, Workpiece vibration augmented wire arc additive manufacturing of high strength aluminum alloy, J. Mater. Process. Technol. 271 (2019) 85-92. https://doi.org/10.1016/j.jmatprotec.2019.03.028
44. G. Tanvir, Md. Abdul Karim, S. Jadhav, S. Islam, Y-M. Kim, H-J. Ryu, D.B Kim, Effect of hot isostatic pressing on porosity of wire-arc directed energy deposited TZM/NbZr1 bimetallic structure, Virtual. Physic. Prototyping. 19:1 (2024) 2404989, https://doi.org/10.1080/17452759.2024.2404989
45. S. Islam, S. Jadhav, T. Park, F. Pourboghrat, X. Fan, P.K. Liaw, D.B. Kim, Crystal plasticity approach for predicting mechanical responses in wire-arc directed energy deposition of NbZr1 refractory alloy, Add. Manufact. 84 (2024) 104107. https://doi.org/10.1016/j.addma.2024.104107
46. S. Jadhav, G.H. Jeong, M.S. Bajestani, S. Islam, H-J. Lee, Y.T. Cho, D.B. Kim, Investigation of surface roughness, microstructure, and mechanical properties of overhead structures fabricated by wire + arc additive manufacturing, Int. J. Adv. Manufact. Technol. 131 (2024) 5001–5021. https://doi.org/10.1007/s00170-024-13330-3
47. C. Wang, W. Suder, J. Ding, S. Williams, The e ff ect of wire size on high deposition rate wire and plasma arc additive manufacture of Ti-6Al-4V, J. Mater. Process. Technol. 288, 2021 116842. https://doi.org/10.1016/j.jmatprotec.2020.116842
48. S. Divinski, F. Hisker, C. Klinkenberg, C. Herzig, Niobium and titanium diffusion in the high niobium-containing Tie54Ale10Nb alloy, Intermetallics 14 (2006) 792-799. https://doi.org/10.1016/j.intermet.2005.12.007
49. R. Pan, J. Xu, Zh. Huang, T. Zhou, Y. Feng, Y. Sun, Sh. Chen, T. Lin, P. He, Interface homogenization control and microstructural analysis of ZrC0.85 joints diffusion bonded using Nb and Ti/Nb/Ti as the interlayer, J. Mater. Res. Technol. 30 (2024) 3535–3546. https://doi.org/10.1016/j.jmrt.2024.04.089
50. Tong Lin, Chun Li, Dejun Gao, Zeshu Du, Xiaoqing Si, Junlei Qi, Jian Cao, Enhanced Ti/Nb/Ti diffusion bonding at ultra-low temperatures by surface nanocrystallization treatment, J. Mater. Sci. Technol 192 (2024) 228–239. https://doi.org/10.1016/j.jmst.2023.12.047
51. S. Chen, F. Ke, M. Zhou, Y. Bai, Atomistic investigation of the effects of temperature and surface roughness on diffusion bonding between Cu and Al, Acta. Mater. 55 (2007) 3169–3175. http://dx.doi.org/10.1016/j.actamat.2006.12.040

52. H. Okamoto, M.E. Schlesinger, E.M. Mueller, ASM Handbook Volume 3: Alloy Phase Diagrams, ASM International, (2016) (ISBN: 978-1-62708-070-5) https://doi.org/10.31399/asm.hb.v03.9781627081634
53. S.D. Chen, A.K. Soh, F.J. Ke, Molecular dynamics modeling of diffusion bonding, J. Scripta Mater. 52 (11) (2005) 1135–1140, https://doi.org/10.1016/j.scriptamat.2005.02.004
54. C. Li, D. Li, X. Tao, H. Chen, Y. Ouyang, Molecular dynamics simulation of diffusion bonding of Al–Cu interface, J. Modell. Simul. Mater. Sci. Eng. 22 (2014) 065013. https://doi.org/10.1088/0965-0393/22/6/065013
55. J. Wei, CH. Xu, P. Li, H. Deng, SH. Xiao, W> Hu, Molecular dynamics simulations of the diffusion characteristics on the Fe-W interfaces system, Fusion. Eng. Des. 159 (2020) 111850. https://doi.org/10.1016/j.fusengdes.2020.111850
56. X. Gan, S. Xiao, H. Deng, X. Sun, X. Li, W. Hu, Atomistic simulations of the Fe (001)–Li solid–liquid interface, Fusion Eng. Des. 89 (2014) 2894–2901. http://dx.doi.org/10.1016/j.fusengdes.2014.06.018
57. Y. Yang, D.L. Olmsted, M. Asta, B.B. Laird, Atomistic characterization of the chemically heterogeneous Al–Pb solid–liquid interface, Acta. Mater. 60 (2012) 4960–4971. http://dx.doi.org/10.1016/j.actamat.2012.05.016
58. N.A. Mara, I.J. Beyerlein, Review: effect of bimetal interface structure on the mechanical behavior of Cu–Nb fcc–bcc nanolayered composites. J. Mater. Sci. 49 (2014) 6497–516. https://doi.org/10.1007/s10853-014-8342-9
59. S. Zheng, J.S. Carpenter, R.J. McCabe, I.J. Beyerlein, N.A. Mara, Engineering interface structures and thermal stabilities via SPD processing in bulk nanostructured metals, Sci. Rep. 4 (2014) 4226. https://doi.org/10.1038/srep04226
60. K.Y. Yu, D. Bufford, C. Sun, Y. Liu, H. Wang, M.A. Kirk, M. Li, X. Zhang, Removal of stacking-fault tetrahedra by twin boundaries in nanotwinned metals, Nat. Commune. 4 (2013) 1377. https://doi.org/10.1038/ncomms2382
61. A.D. Brailsford, R. Bullough, The theory of sink strengths. Philos Trans R Soc Lond Ser A – Math Phys. Eng. Sci. 302 (1981) 87–137. https://doi.org/10.1098/rsta.1981.0158
62. A.P. Sutton, R.W. Balluffi, Interfaces in crystalline materials. Oxford: Oxford University Press; (1995).
63. J.W. Gibbs, The Scientific Papers. Volume One. Thermodynamics (Dover, New York, 1961)
64. R. Alexander, M.-C. Marinica, L. Proville, F. Willaime, K. Arakawa, M. R. Gilbert, S. L. Dudarev, Ab initio scaling laws for the formation energy of nanosized interstitial defect clusters in iron, tungsten, and vanadium, Physic. Rev. B 94, (2026) 024103. https://doi.org/10.1103/PhysRevB.94.024103
65. M.P. Harmer, The phase behavior of interfaces, Sci. 332 (2011) 182–3. https://doi.org/10.1126/science.1204204
66. M.S. Hasan, R. Lee, W.W. Xu, Deformation nanomechanics and dislocation quantification at the atomic scale in nano-polycrystalline magnesium. J. Mag. Alloy. 8 (2020) 1296–1303. https://doi.org/10.1016/j.jma.2020.08.014
67. X. Zhou, Y. Chen, Y. Huang, Y. Mao, Y. Yu, Effects of niobium addition on the microstructure and mechanical properties of laser-welded joints of NiTiNb and Ti6Al4V alloys, J. Alloy. Comp (2017), https://doi.org/10.1016/j.jallcom.2017.11.307
68. M. Piao, S. Miyazaki, K. Otsuka, N. Nishida, Effects of Nb addition on the microstructure of Ti-Ni alloys, Mater. Trans., JIM 33 (1992) 337–345. https://doi.org/10.2320/matertrans1989.33.337
69. V. Jindal, F. Shahedipour-Sandvik, Density functional theoretical study of surface structure and adatom kinetics for wurtzite AlN, J. Appl. Phys. 105 (2009). https://doi.org/10.1063/1.3106164

70. S.F. Hwang, Y.H. Li, Z.H. Hong, Molecular dynamic simulation for Cu cluster deposition on Si substrate, Comput. Mater. Sci. 56 (2012) 85–94, https://doi.org/10.1016/j.commatsci.2012.01.010

67. H. Mes-adi, Y. Lachtioui, K. Saadouni, M. Mazroui, Morphology and surface properties of Cu thin film on Si (001), Thin Solid Films 698 (2020) 137853. https://doi.org/10.1016/j.tsf.2020.137853

72. L. Tian, Y. Zhang, C. Wang, L. Quan, H. Yu, X. Zheng, Y. Yang, Effect of dislocation loops formed during cyclic deformation on the microstructural characteristics and mechanical behavior of 2524 aluminum alloy, Materials Science & Engineering A, https://doi.org/10.1016/j.msea.2026.149758.

73. Jan Fikar, Robin Schäublin, Daniel R. Mason, Duc Nguyen-Manh, Nano-sized prismatic vacancy dislocation loops and vacancy clusters in tungsten, Nuclear Materials and Energy 16 (2018) 60–65. https://doi.org/10.1016/j.nme.2018.06.011

74. [4] Mugilgeethan VIJENDRAN, Ryosuke MATSUMOTO, Transition between a nano-sized prismatic dislocation loop and vacancy cluster in α-iron: An atomic scale study, Computational Materials Science 225 (2023) 112195. https://doi.org/10.1016/j.commatsci.2023.112195

75. D. Hull, G.J. Bacon, Introduction to dislocations, 5th edn. Butterworth-Heinemann, London, (2011).

76. B.B. Vanani, M. Abbasi, A. Abdollahzadeh, A new investigation on graphene-reinforced 304L nanocomposite made by additive manufacturing process: Microstructure and tribology study, J. Mater. Res. Technol. 32 (2024) 674-686. https://doi.org/10.1016/j.jmrt.2024.07.137

77. X.SH. Kong, X. Wu, Y.W You, C.S. Liu, Q.F. Fang, J.L. Chen, G.N. Luo, Zh. Wang, First-principles calculations of transition metal–solute interactions with point defects in tungsten, Acta Mater 66 (2014) 172–183. https://doi.org/10.1016/j.actamat.2013.11.044

78. I. Ipatova, R.W. Harrison, P.T. Wady, S.M. Shubeita, D. Terentyev, S.E. Donnelly, E. Jimenez-Melero, Structural defect accumulation in tungsten and tungsten-5wt.% tantalum under incremental proton damage, J. Nucl. Mater. 501 (2018) 329–335. https://doi.org/10.1016/j.jnucmat.2017.11.030

79. H.J. Chu, E. Pan, X. Han, J. Wang, I.J. Beyerlein, Elastic fields of dislocation loops in three-dimensional anisotropic biomaterials, J. Mech. Phys. Solid. 60 (2012) 418–431. https://doi.org/10.1016/j.jmps.2011.12.007

80. X. Zhang, Z. Xiong, L. Li, Zh. Feng, B. Wu, M. Li, CH. Zhao, L. Zhang, Dislocation loops enhance wear resistance in $Ti_2Zr_{0.75}NbV_x$ lightweight refractory medium-entropy alloys via high thermal conductivity-promoted oxide film formation, Int. J. Ref. Metal. Hard. Mater. 132 (2025) 107239. https://doi.org/10.1016/j.ijrmhm.2025.107239

81. H. Amini, P. Gholizadeh, E. Poursaeidi, J. Davoodi, A molecular dynamics simulation of Ti–TiN multilayer deposition on FeCrNi(001) alloy substrate, Vacuum 193 (2021) 110519. https://doi.org/10.1016/j.vacuum.2021.110519

82. S. Yin, Y. Zuo, A. Abu-Odeh, H. Zheng, X.G. Li, J. Ding, S.P. Ong, M. Asta, R. O. Ritchie, Atomistic simulations of dislocation mobility in refractory high-entropy alloys and the effect of chemical short-range order, Nat. Commun. 12 (2021) 4873, https://doi.org/10.1038/s41467-021-25134-0

83. X. Liu, D. Hua, Y. Shi, Z. Huang, Q. Zhou, S. Li, H. Wang, Dislocation patterning in the TiZrVTa refractory high-entropy alloy under tribological loading, Tribol. Int. 187 (2023) 108740, https://doi.org/10.1016/j.triboint.2023.108740

Declaration of interests

☒ The authors declare that they have no known competing financial interests or personal relationships that could have appeared to influence the work reported in this paper.

☐ The authors declare the following financial interests/personal relationships which may be considered as potential competing interests: